Electrochimica Acta 203 (2016) 379–387

Contents lists available at ScienceDirect

Electrochimica Acta

journal homepage: www.elsevier.com/locate/electacta

Simulation of the role of vibration on Scanning Vibrating Electrode Technique measurements close to a disc in plane

Olga Dolgikh[a], Andrei–Stefan Demeter[a,b,*], Sviatlana V. Lamaka[c,d], Maryna Taryba[c], Alexandre C. Bastos[e], Marcela C. Quevedo[e], Johan Deconinck[a]

[a] Vrije Universiteit Brussel, Research Group Electrochemical and Surface Engineering, Pleinlaan 2, 1050 Brussels, Belgium
[b] Technical University of Cluj Napoca, Faculty of Electrical Engineering, 26-28 George Baritiu Street, 400027 Cluj Napoca, Romania
[c] Centro de Química Estrutural, Instituto Superior Técnico, Universidade de Lisboa. Av. Rovisco Pais, 1049-001 Lisbon, Portugal
[d] MagIC, Magnesium Innovation Centre, Institute of Materials Research, Helmholtz-Zentrum Geesthacht, 21502, Germany
[e] University of Aveiro, CICECO, Department of Materials and Ceramic Engineering, 3810-193 Aveiro, Portugal

ARTICLE INFO

Article history:
Received 1 October 2015
Received in revised form 24 January 2016
Accepted 25 January 2016

Keywords:
SVET
Local mixing
numerical simulations
multi-ion model
concentration gradients

ABSTRACT

An elegant and accessible way to account for the local stirring created by the vibration of the SVET tip by adding a new diffusion–like term into the molar flux expression is proposed, in order to avoid solving the fluid flow. This term is maximal in the point of vibration and rapidly decreases with the distance. It is shown that the local mixing leads to a substantial increase of the migration current density in the vicinity of the probe with simultaneous decrease of the diffusion current contribution. This local mixing has no effect on the pH distribution, regardless the applied polarization, and increases under cathodic polarization the oxygen concentration only when the probe is close to the electrode surface which is confirmed by experimental observations. The proposed model is compared with the analytical current density distributions obtained from potential model and experimental data. All this indicates that local mixing might explain why the SVET technique, although based on the measurement of an ohmic current density, measures always the total current density.

1. Introduction

Scanning Vibrating Electrode Technique (SVET) has become a widely used investigation technique in the field of corrosion [1–6]. It is used primarily for visualization of the corrosion process progression in terms of anodic and cathodic areas localization and evolution in time, as well as current magnitude monitoring.

An ideal analytical tool should not disturb the system under investigation. In practice, the local stirring of the electrolyte is a feature of SVET. This stirring was observed since the introduction of the modern vibrating probe [7]. The main effect of the stirring is the local mixing of the electrolyte, canceling out the concentration gradients. Even at small vibration amplitude (about one diameter of the SVET tip) and moderate vibration frequency, the mixing effect spreads over an area of few times the vibration amplitude. The reduction of the local concentration gradients increases the local electrical potential gradient [8,9]. On the other hand, larger values of the vibration amplitude lead to important increase in the rates of the electrode reactions taking place under diffusion control, e.g the oxygen reduction reaction on cathode [10]. A deeper investigation of this phenomenon performed by one of the authors, proved that in normal operating conditions (SVET tip of diameter 10–20μm placed at more than 50 μm above the surface of the sample, vibration amplitude of the same order of magnitude as the tip radius and up to 200 Hz vibration frequency [11,12]) most of the stirring of the electrolyte solution is caused by the movement of the probe during scanning and less than 5% of the total increase of the cathodic current is caused by the vibration of the tip of the SVET probe [13]. Despite of these disturbances, the technique was experimentally validated long time ago and used to produce valuable analytical results ever since H. Isaacs has adapted SVET for corrosion research [14].

The technique is based on a simple idea: the electrolyte potential in the solution is measured at two different points and then converted to a local current density in the solution, using Eq. (1)

$$\vec{j}_{\mathrm{loc}} = -\kappa \frac{\Delta U}{\Delta \vec{r}} \approx -\kappa \vec{\nabla} U, \tag{1}$$

* Corresponding author.
E-mail addresses: Olga.Dolgikh@vub.ac.be (O. Dolgikh), andrei.demeter@et.utcluj.ro (A. Demeter), sviatlana.lamaka@hgz.de (S.V. Lamaka), mgtaryba@gmail.com (M. Taryba), acbastos@ua.pt (A.C. Bastos), marcelacitlalimreyes@ua.pt (M.C. Quevedo), Johan.Deconinck@vub.ac.be (J. Deconinck).

http://dx.doi.org/10.1016/j.electacta.2016.01.188
0013-4686/

where j_{loc} ($A\,m^{-2}$) is the local current density in the electrolyte, κ ($S\,m^{-1}$) is the local electrolyte conductivity, ΔU (V) the electrical potential difference between the points at the distance $\Delta\vec{r}$ (m). This provides a good approximation of the gradient of the electric potential in solution, $\vec{\nabla}U$ ($V\,m^{-1}$) in the direction of $\Delta\vec{r}$, which corresponds to the peak-to-peak vibration amplitude in the direction of the measurement. Conductivity of the electrolyte solution is assumed to be constant. Most often it is believed that SVET measures the total current in a measuring point. However, this is true only far from the electrode, outside the diffusion layer where migration is dominant. Most of the corrosion studies are performed at distances between 50 and 150 μm from the surface of the electrode, while the usual thickness of the diffusion layer in quiescent conditions is higher than 200 μm. It is expected that measuring in the diffusion layer would lead to significant discrepancies between the measured migration current and the total current and even to seemingly unbalanced anodic and cathodic currents [10,15]. This apparent imbalance could be explained either by the presence of a chemical redox reaction that influences the probe/solution potential [15] or by the enhancement of the dissolved oxygen transport by the moving SVET probe [13]. Further, deviations are observed between the measured and the simulated current densities above real corroding samples and these deviations are more pronounced in the case of a Multi-Ion model than of the Potential (electrostatic) model. This leads to an astonishing conclusion that the Potential model would be better suited for simulation of SVET measurements than the Multi–ion model [16]. The question arises: "Why is a Multi-ion model, which encompasses the electrostatic model, less accurate than a Potential model"?

The possible answer resides in the fact that none of the above mentioned models, however complex it is, accounts for the convection created by the movement of the SVET probe. At the same time, it is true that a proper, quantitative simulation of the SVET probe movement (translation and vibration) would be way too complex and time consuming for everyday electrochemical practice. In what follows, we will present a simplified approach to account for the mixing effect around the tip of the SVET probe, without actually solving for the convection created by its vibration in the electrolyte solution. The effects of the probe movement during scanning were omitted at this time, as they can be mitigated by a suitable set up of the scanning procedure. The proposed approach brings the simulated SVET response obtained with use of a Multi-ion model closer to the measured one. The validation is performed by comparing the results of the simulations with the analytical current density distribution and with a set of actual SVET measurements.

2. Theoretical approach

2.1. Potential model

The Potential model assumes perfect mixing of the electrolyte solution, therefore no concentration gradients:

$$div\left(-\kappa\vec{\nabla}U\right)=0, \tag{2}$$

with κ being the electrical conductivity of the electrolyte:

$$\kappa=F^2\sum_i z_i^2 u_i c_i = const. \tag{3}$$

Here $F=96485\,C\,mol^{-1}$ is the Faraday's constant, c_i ($mol\,m^{-3}$), z_i and $u_i=D_i/RT$ ($mol\,s\,kg^{-1}$) are concentration, charge and mobility of species i respectively. Total current density in the solution is given by the gradient of the electrical potential only, Eq. (4).

$$j=-\kappa\vec{\nabla}U. \tag{4}$$

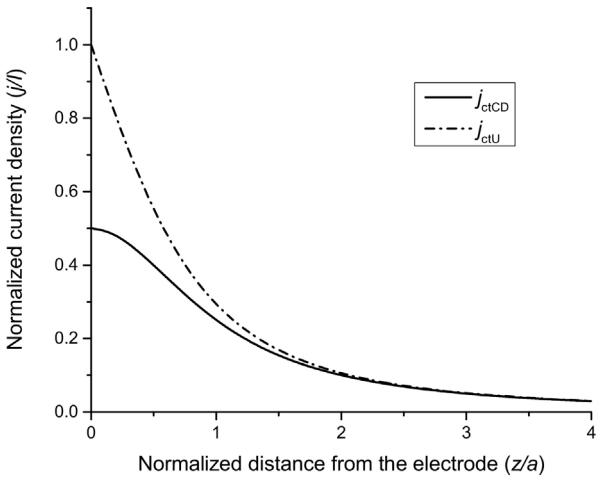

Fig. 1. Theoretical current density distributions, normalized to the total current I, above the center of the electrode for the limiting cases of equipotential (Eq. (5)) and constant current density (Eq. (6)) electrodes.

Two theoretical limiting cases are possible for the current density distribution above a disk-shaped electrode: an equipotential electrode and a constant current density electrode. If we restrict the analysis to the center of the electrode in polar coordinates, analytical expressions describing the current density distribution as a function of the distance from the surface of the electrode are available for these cases (Eq. (5) for the equpotential and Eq. (6) for the constant current density electrodes respectively) [17,18]. Since in corrosion studies mainly the vertical component of the current density is reported, in what follows we will consider only this z-component in the center of the disc:

$$j_{ctU}=-\frac{I}{2\pi\kappa}\frac{1}{(a^2+z^2)} \tag{5}$$

$$j_{ctCD}=-\frac{I}{a^3\kappa\pi}\left(\frac{z}{\sqrt{1+(z/a)^2}}+a\right) \tag{6}$$

with I (A) the total current, a (m) the radius of the electrode and z (m) the distance from the surface of the electrode. A graphical representation of these two extreme current density distributions is given in Fig. 1. The real (measured) current density distribution is expected to fall between the two theoretical ones.

2.2. Multi–ion model

The mathematical model for ion transport in dilute solutions based on balance equations provides concentration and potential distributions (Eq. (7)) and ensures the electroneutrality of the solution (Eq. (8)) [19].

$$\frac{\partial c_i}{\partial t}+\vec{v}\cdot\vec{\nabla}c_i=\vec{\nabla}\left(z_i F u_i c_i\vec{\nabla}U+D_i\vec{\nabla}c_i\right)+R_i, \tag{7}$$

$$\sum_i z_i c_i=0. \tag{8}$$

The notations in the above equations have the following meaning: $\vec{v}$ ($m\,s^{-1}$) the velocity field of the electrolyte solution, D_i ($m^2\,s^{-1}$) the diffusion coefficient of the species i and R_i ($mol\,m^{-3}s^{-1}$) the net production rate of species i due to homogenous reactions, given by Eq. (9)

$$R_i=\sum_i \nu_k s_{ki} \tag{9}$$

with v_k (mol m^{-3} s^{-1}) the rate of a homogeneous reaction k, s_{ki} the stoichiometric coefficient of species i in this reaction. For species not involved in any homogenous reactions, the contribution to the mass balance R_i is zero.

Total current density in the electrolyte is the sum of normal fluxes of species $\vec{N}_i$ multiplied by z_iF:

$$j_{\text{tot}} = \sum_i z_i F \vec{N}_i = F\sum_i z_i c_i \vec{v} - F\sum_i z_i D_i \vec{\nabla} c_i - \frac{F^2}{RT}\sum_i z_i^2 D_i c_i \vec{\nabla} U. \tag{10}$$

Due to the electroneutrality condition, convection contribution in the Eq. (10) cancels out, and current in the electrolyte is transported by diffusion and migration only

$$j_{\text{tot}} = \underbrace{F\sum_i z_i D_i \vec{\nabla} c_i}_{j_{\text{diff}}} - \underbrace{\kappa \cdot \vec{\nabla} U}_{j_{\text{migr}}}. \tag{11}$$

However, one cannot neglect the convection term, even for a quiescent electrolyte, because it is responsible for the establishment of the diffusion layer just above the electrode surface. Inside this layer, both potential and concentration gradients exist, the latter being the predominant ones, especially for concentrated electrolytes and/or fast electrode reactions. The use of Multi–Ion model is required in order to adequately describe the phenomena that take place in this zone. Outside the diffusion layer, the electrolyte is perfectly mixed and no concentration gradients exist. Hence, $j_{\text{tot}} \approx j_{\text{migr}}$ and the Potential model is fully applicable.

In the simulations, if the fluid velocity $\vec{v}$ is set to zero, the diffusion layer extends up to the top boundary of the computational domain, and the simulated value of the limiting current becomes dependent on the chosen domain height, which is physically wrong. In order to overcome this problem one has a choice either to solve often unknown fluid flow [20,21] or to make an artificial separation of the electrolyte into diffusion layer and a bulk [16]. A third approach, introduced by Amatore [22] and further developed for multi-ion systems by some of the authors [23] implies the use of numerical approximations to mimic the effect of the flow, without actually solving it. This approach uses a concept of so-called micro convection that is always present even in stagnant electrolytes due to the small local temperature differences, evaporation, vibrations etc. The micro convection is mathematically expressed by a diffusion-like term $\vec{N}_{\mu\text{conv}} = -D_{\mu\text{conv}}\vec{\nabla} c_i$ with $D_{\mu\text{conv}}$ being space-dependent species-independent micro convection coefficient:

$$D_{\mu\text{conv}} = D_{\text{ref}}\left(z/\delta_{\text{ref}}\right)^4, \tag{12}$$

where D_{ref} and δ_{ref} are the molecular diffusion constant and the thickness of the diffusion layer for a reference species respectively.

In the frame of this concept, expression for the total current in the electrolyte (Eq. (10)) transforms into

$$j_{\text{tot}} = F\sum_i z_i (D_i + D_{\mu\text{conv}})\vec{\nabla} c_i - \kappa \cdot \vec{\nabla} U. \tag{13}$$

The coefficient $D_{\mu\text{conv}}$ is zero at the electrode surface and increases rapidly outside the diffusion layer (see Fig. 2). For an electrolyte bulk, where $D_i \ll D_{\mu\text{conv}}$,

$$j_{\text{tot}} \approx FD_{\mu\text{conv}}\vec{\nabla}\sum_i z_i c_i - \kappa \cdot \vec{\nabla} U \approx j_{\text{migr}}. \tag{14}$$

and micro convection acts just like the classical convection mixing the electrolyte. Thus, by use of the micro convection concept, a natural smooth passage is made from the diffusion dominated region next to the electrode to the migration dominated electrolyte bulk.

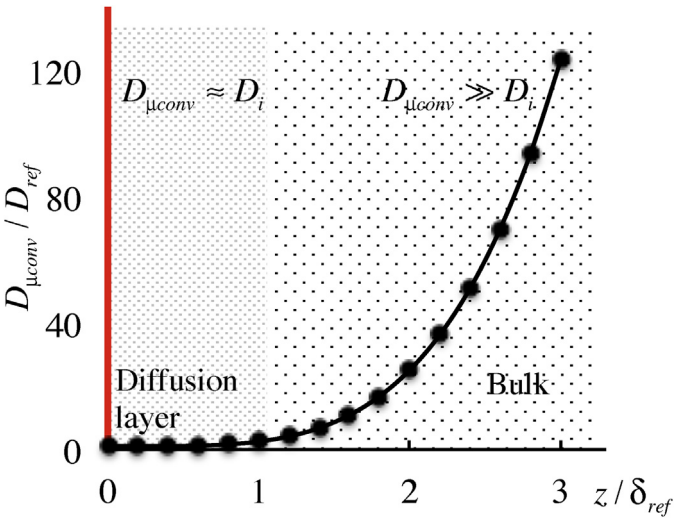

Fig. 2. Dependence of the micro-convection coefficient on the distance from the electrode.

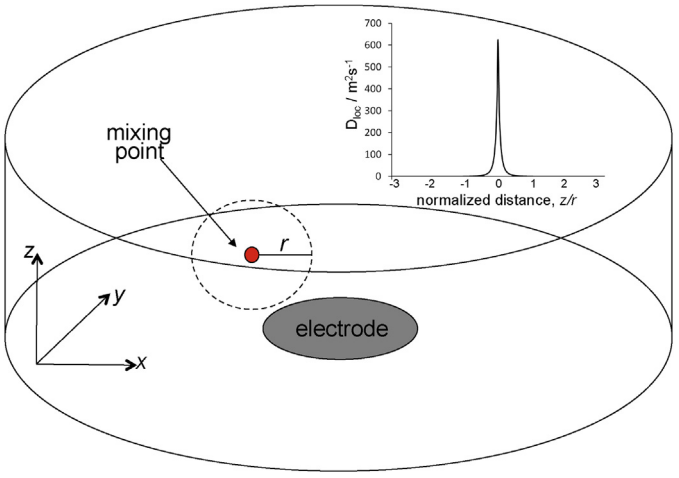

Fig. 3. The position of the SVET tip and the stirred sphere around it. Inset: the shape of the local equivalent diffusion D_{loc} as a function of the normalized distance from the SVET tip.

2.3. Local mixing model

Starting from the micro convection concept, we can apply an identical mixing effect, in a well defined area around a point. Let us consider the SVET tip as a point with coordinates x_0, y_0, z_0 located inside the electrolyte volume (see Fig. 3). The mixing effect created by the vibration of the tip spreads over a sphere of radius r and then vanishes. Mathematically, the mixing around the SVET tip can be mimicked by adding an equivalent diffusion term $D_{\text{loc}}\vec{\nabla} c_i$, that becomes very large at the mixing point and is negligible at a distance r. For every point in the electrolyte, the equivalent diffusion coefficient D_{loc} can be described by the following expression:

$$D_{\text{loc}} = D_{\text{ref}}\left(\frac{r}{f\cdot r + \sqrt{(x_0-x)^2+(y_0-y)^2+(z_0-z)^2}}\right)^p \tag{15}$$

with D_{ref} the molecular diffusion constant, the same as for micro convection, f a constant, x_0, y_0, z_0 (m) the coordinates of the SVET tip, x, y, z (m) the local coordinates, r (m) the distance over which the local mixing is active, p an integer power, larger than zero. The evolution of D_{loc} with the distance from the mixing point is shown in the inset of Fig. 3.

When the local mixing is considered, Eq. (7) transforms into

$$\frac{\partial c_i}{\partial t} = \vec{\nabla}\left(\left[D_i + D_{\mu\mathrm{conv}} + D_{\mathrm{loc}}\right]\vec{\nabla}c_i + \frac{z_i F D_i c_i}{RT}\vec{\nabla}U\right) + R_i, \quad (16)$$

Eq. (16) accounts for all transport phenomena expected to take place in a quiescent electrolyte: diffusion under the influence of the concentration gradients, micro convection with formation of the diffusion layer, local mixing at the position of the SVET tip, and migration of the charged species under the influence of the electric field.

Total current density in the electrolyte is then given by the expression:

$$j_{\mathrm{tot}} = F\sum_i z_i(D_i + D_{\mu\mathrm{conv}} + D_{\mathrm{loc}})\vec{\nabla}c_i - \kappa\cdot\vec{\nabla}U. \quad (17)$$

In the mixing point $D_{\mathrm{loc}} \gg D_i$ and, by analogy with Eq. (13), total current becomes almost equal to the migration current:

$$j_{\mathrm{tot}} \approx FD_{\mathrm{loc}}\vec{\nabla}\sum_i z_i c_i - \kappa\cdot\vec{\nabla}U \approx j_{\mathrm{migr}}. \quad (18)$$

Note that this effect is very local as D_{loc} becomes comparable to the molecular diffusion coefficient already at the distance r from the center of the probe – see Eq. (15) – but can substantially influence locally the contribution of the migration current density in total current.

Governing equations (8) and (16) were solved using a Finite Element Method modeling software *MuPhyS*. This software has been developed as a collective effort at the Research Group Electrochemical and Surface Engineering of Vrije Universiteit Brussel.

3. Experimental

3.1. SVET measurements

Ionic currents densities in solution were measured using SVET technique. Commercially available system manufactured by Applicable Electronics and controlled by the ASET program (Sciencewares), was used to perform the SVET and local pH measurements. The Parylene C insulated Pt-Ir microelectrodes with 5 μm exposed apex were purchased from Microprobes Inc. A platinum black was electrodeposited on the tip to the final diameter of 18 μm. The microelectrode vibrates in two directions (z and x) but only the z vibration (vertical component) was considered in the present study. The frequency was 126 Hz and the amplitude of vibration was 36 μm peak to peak. Before carrying out experimental work the calibration procedure was performed using a point current source (glass capillary with a tip diameter of 2 μm). Calibration was recorded at 150 μm distance between the vibrating probe and a current source while passing current of 60 nA [7,24]. The calibration is valid for different solutions provided that the software is updated with the correct conductivity/resistivity of solution. The time of acquisition was of 0.2 s in each point with prior waiting time of 0.15 s to avoid translation effects from the previous position. The measurements were carried out in both 0.05 M and 0.005 M NaCl solutions.

3.2. Local pH measurements

Current density and pH measurements were acquired sequentially. The localized pH measurements were performed using pH-selective glass-capillary microelectrodes with the diameter of the tip 1.8 ± 0.2 μm. In order to prepare the microelectrodes, silanized glass micropipettes were back-filled with the inner filling solution (0.01 M KH_2PO_4 + 0.1 M KCl) and tip-filled with the H^+–selective ionophore–based membrane. The membrane was composed of 6 wt.% 4–nonadecylpyridine, 12 mol.% potassium tetrakis(4–chlorophenyl) borate and membrane solvent 2–nitrophenyloctyl ether. All reagents for the pH–selective membrane were Selectophore grade products from Fluka. The column length of the membrane was about 60–70 μm. A chlorinated silver wire was inserted into the inner filling solution as the internal reference electrode. More detailes of the preparation procedure can be found elsewhere [25].The microelectrodes demonstrated a stable and reproducible potential in the pH range 2.0 to 10.6 with a linear response slope of -54.8 ± 0.7 mV/pH. A move–wait–measure pH scheme was employed for measuring above the surface. The time for acquisition for each pH data–point was 1.5 s.

3.3. Dissolved oxygen measurements by the micro-optode

Line scan measurements of concentration of dissolved oxygen above Pt disk were performed using FireStingO2 fibre-optic oxygen meter OXR50 (Pyroscience^{TM}) [26,27]. The needle-like retractable optic fiber of 50 micron diameter was placed in a rigid steel guide constituting the micro-optode. The micro-sensor employs an O_2-sensitive indicator immobilized on the tip of the sensor. The indicator is excitable with orange-red light at a wavelength of 610–630 nm and demonstrates an oxygen dependent luminescence at 760–790 nm. The measuring principle is based on a sinusoidally modulated red excitation light causing a phase-shifted sinusoidally modulated emission in the NIR. The phase-shift is recorded and is converted into oxygen units based on the Stern–Volmer theory. The sensitivity of the micro-optode is 0.01 ppm. The calibration of the micro-optode controlled by PyroOxygenLogger software was performed using N_2 (0%DO) and air (20.9% DO) saturated solutions.

3.4. Rotating Disk Electrode measurements

Polarization curves for fitting the kinetic parameters of the electrode reactions were obtained by using Rotation Disk Electrode (RDE). RDE measurements were done in a conventional one–compartment glass cell of 100 ml volume in NaCl solution. A Radiometer Analytical EM–EDI–PT–D2 RDE with a radius of 1 mm was used. Polarization curves in positive and negative direction were recorded separately, from 0 V to −2.24 V (SCE) and −0.44 V to 1.76 V (SCE) at the rate of 10 mV/s. The rotation speed of the electrode was adjusted at 100, 500, 1000, 2000, 2500, 3000, 4000 rpm using a Pine AFCPRB rotator. The measurements were performed at 21°C (294 K) in either 0.05 M (pH = 6.78) or 0.005 M (pH = 5.86) NaCl solution.

3.5. Materials

Local current density and pH were measured over a platinum disc electrode embedded in epoxy holder. The diameter of the Pt disk was 270 μm. A positive or negative current of 60 nA was injected into the wire making it a source of current. The optical micrographs showing the current source with either SVET or pH probes are presented in Fig. 4.

4. Multi-Ion model description

4.1. Electrochemical system

Two electrolyte solutions often used in corrosion studies – 0.005 M and 0.05 M NaCl – were considered, containing five relevant species: H^+, OH^-, Na^+, Cl^- and O_2. Their initial (bulk) concentrations, charge numbers and diffusivities are given in Table 1. The diffusion coefficients of the species are taken from the

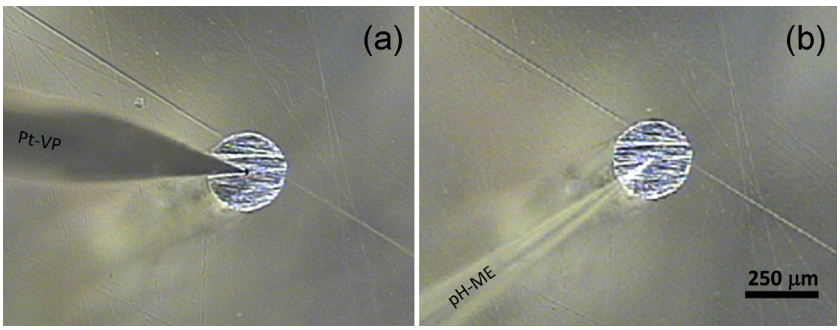

Fig. 4. Optical micrographs of the Pt disk current source together with vibrating probe (a) and pH-selective glass-capillary micro-electrode (b).

Table 1
Bulk concentration, charge numbers and diffusivities of the species considered in the model

species	c_{bulk}, mol m^{-3}	z	$D \times 10^9$, m^2 s^{-1}
Na^+	5/50	+1	1.26/1.13
Cl^-	5/50	−1	1.93/1.72
H^+	1.00×10^{-3}	+1	9.31
OH^-	1.00×10^{-6}	−1	5.26
O_2	0.26	0	2.1

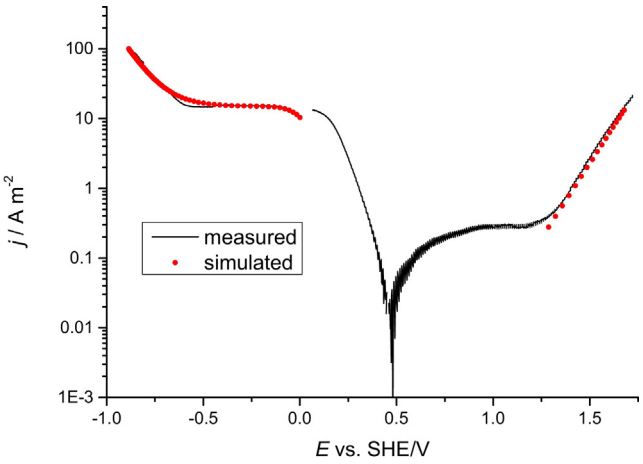

Fig. 5. Experimental polarization curve obtained on Pt rotating disc electrode in 0.005 M NaCl electrolyte. Rotation speed 2000 rpm. Simulated parts of the anodic and cathodic branches are shown as dots.

literature for the infinite diluted solutions [19] and those of Na^+ and Cl^- are slightly adjusted to match the measured conductivity (0.543 and 0.061 S mv^{-1} for 0.05 M and 0.005 M NaCl solutions respectively).

It is assumed the oxygen reduction reaction (Eq. (19)) and proton reduction (Eq. (20)) take place on the surface of the working electrodes in the case of the cathodic polarization, while the direct water oxidation (Eq. (21)) occurs under anodic polarization. All three reactions are considered to be irreversible.

$$H_2O + O_2 + 4e^- \longrightarrow 4OH^-, \quad (19)$$

$$2H^+ + 2e^- \longrightarrow H_2, \quad (20)$$

$$2H_2O \longrightarrow O_2 + 4H^+ + 4e^-. \quad (21)$$

The kinetic parameters for these electrode reactions in the potential ranges of interest were first estimated from the experimentally measured polarization curves (Fig. 5) using Tafel equation. Then these parameters were further fitted together with the value of the micro convection parameter δ_{ref} by performing the full milti-ion model simulations and comparing the thus obtained

Table 2
Kinetic parameters of the electrode reactions considered in the model

Reaction	k_{ox}	α_{ox}	k_{red}	α_{red}
$H_2O + O_2 + 4e^- \longrightarrow 4OH^-$	0	0	3.5×10^{-4}	0.13
$2H^+ + 2e^- \longrightarrow H_2$	0	0	5.0×10^{-8}	0.13
$2H_2O \longrightarrow O_2 + 4H^+ + 4e^-$	2.5×10^{-12}	0.065	0	0

Table 3
Contribution of the migration current density j_{migr} to the total current density j_{tot} at 100 µm above the center of the electrode simulated for different sets of local mixing parameters r, p, f (Eq. (15))

Parameter		j_{migr}/j_{tot}, %					
p		2			4		
r		20	30	50	20	30	50
f	0.1	30	38	48	56	75	87
	0.2	26	31	49	42	65	70
	0.25	24	29	35	36	48	62

polarization curve with the measured one. For practical reasons molecular oxygen was chosen as a reference species for the micro convection contribution such that $D_{ref} = 2.1 \times 10^{-9}$ m^2 s^{-1}. The best agreement with the measurements was obtained for $\delta_{ref} = 230$ µm and kinetic parameters of the electrode reactions (19)–(21) listed in Table 2.

The only chemical reaction considered in the model is water dissociation ($H_2O \rightleftharpoons H^+ + OH^-$), with $k_f = 2.71$ s^{-1} and $k_b = 1 \times 10^{-4}$ m^3 mol^{-1} s^{-1} [28].

4.2. Parameters for local mixing contribution

For the local mixing contribution, three unknown parameters that influence the local mixing factor appear in Eq. (15): the radius of the mixing sphere r, the power p, and the factor f. In order to asses the effect of these parameters and to choose the optimal combination, a parametric study was performed. Arbitrary values in a reasonable range (educated guess) were allocated to each parameter: $r = 20$, 30 and 50 µm, $p = 2$ and 4, $f = 0.1$, 0.2 and 0.25. The position of the mixing point was fixed at 100 µm above the center of the electrode. One simulation was performed for the reference case with no local mixing and one for each combination of parameters. The effect of the mixing was quantified by the contribution of the migration current density to the total current density, in percents. The results obtained are presented in Table 3.

For the reference case, the contribution of the migration to the total current density was 14%. As one can observe in Table 3, the lowest migration contribution to the total current density is predicted for $f = 0.25$, $p = 2$ and $r = 20$ µm, just 24%, while for $r = 50$ µm, $p = 4$ and $f = 0.1$ we have the highest contribution, 87%. However, given the relatively low vibration amplitude used to acquire the

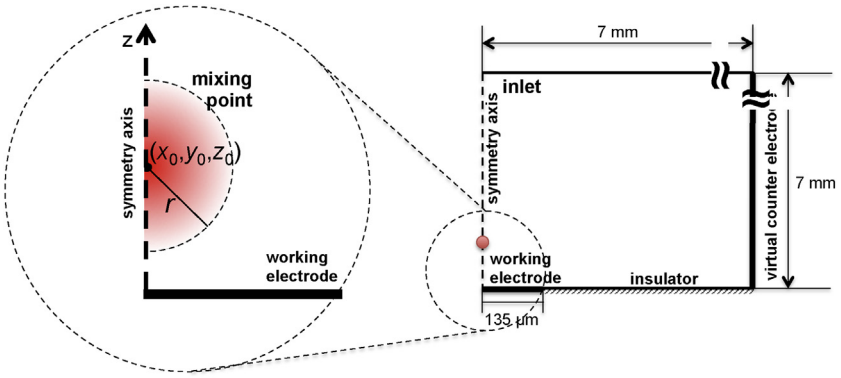

Fig. 6. Axisymmetrical geometry used for simulations.

SVET data presented in this work, the following combination of parameters $r = 30\ \mu m$, $p = 4$ and $f = 0.1$ was used in all subsequent simulations in order to illustrate the effect of local mixing.

4.3. Geometry and boundary conditions

The electrode configuration used in this work is schematically shown in Fig. 3. A 270 µm Pt disk is submerged under the layer of the electrolyte with 7 mm thickness. In order to be able to compare the simulation results against the analytical current density distributions, the analysis of the current density distribution will be restricted to the vertical line passing through the center of the electrode. This allows to reduce the real 3D geometry to an axisymmetrical computational domain. As we are interested in the phenomena taking place above the electrode, and the concentration gradients are restricted to few hundred micrometers around it, we consider only a cylindrical area with a radius of 7 mm around the electrode depicted in Fig. 6.

The left side wall is the symmetry axis, the right side wall acts as a virtual electrode where constant concentration of species and zero electrolyte potential are imposed. The top boundary is an inlet for oxygen. The insulator is placed next to the working electrode on the bottom of the domain. The potential applied on the working electrode was chosen in such way that the resulting current is 60 nA, meaning an average current density of 1.05 A m^{-2}.

5. Results and discussion

Current density distributions along the electrode radius simulated for the reference case (no local mixing) are shown in Fig. 7. In case of anodic polarization, the simulations predict a constant current density (less than 1% variation from center to the edge) while for cathodic polarization the predicted magnitude of the current density in the center of the electrode is 23% lower than on the edge. The influence of the electrolyte concentration is below 1%, therefore in what follows we will present the results for 0.05 M NaCl only. Based on these results one would expect to have the anodic current density distribution in electrolyte close to the constant current analytical distribution (Eq. (6)). For the cathodic current density distribution this is not really the case and it is expected to be in a condition that is in between constant current density and isopotential conditions (Eq. (5)).

Current density profiles above the center of the electrode simulated for the reference case for anodic and cathodic polarizations are compared with the corresponding SVET measurements and the analytical distributions for isopotential and constant current density electrodes in Fig. 8. As one can observe in Fig. 8(a), under anodic polarization, both simulated (j_{tot}) and measured current densities overlap the analytical current density distribution corresponding

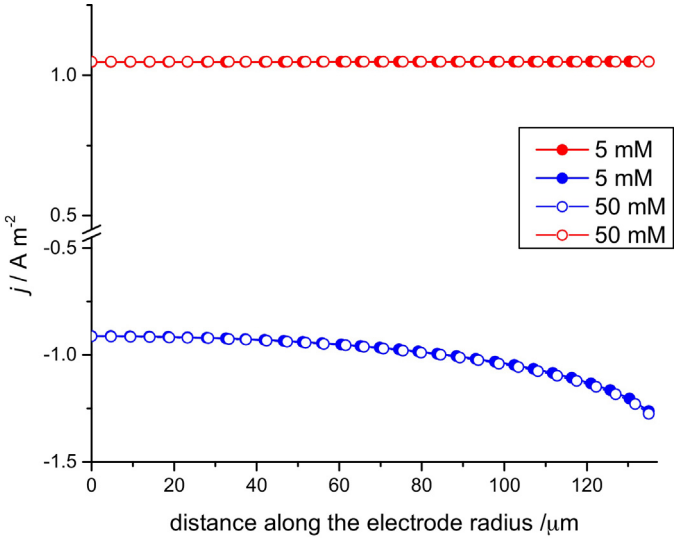

Fig. 7. Simulated current density distributions along the electrode in case of anodic (red lines) and cathodic (blue lines) polarization ($I = \pm 60$ nA) for 5 and 50 mM NaCl solutions. The probe is located 100 µm above the electrode. Local mixing is not taken into account.

to the constant current density disk situation in full agreement with the data of Fig. 7. Surprisingly, a similar current distribution is obtained for the cathodic polarization as well, see Fig. 8(b), despite the fact that based on the current density distribution along the surface one would expect to have the total current density distribution closer to the isopotential analytical current density distribution. In Fig. 8, the simulated diffusion (j_{diff}) and migration (j_{migr}) current components are also shown. One can see that for both anodic and cathodic polarizations, up to $z = 350\ \mu m$, the current transport is dominated by the diffusion. Above this point, the diffusion contribution decreases asymptotically towards zero and the migration current density takes over the current transport.

In order to assess the effect of the local mixing caused by the SVET tip vibration, the simulations were performed for four different positions relative to the electrode and the diffusion layer, considered to be relevant: close to the electrode (30 µm), inside the diffusion layer (100 µm), at the border of the diffusion layer (250 µm) and outside of it (450 µm). The results obtained for both anodic and cathodic polarization are shown in Fig. 9.

The most important consequence of accounting for the local mixing is the local increase of the migration (ohmic) current density. As one can observe in Fig. 9, j_{migr} has maxima in the mixing points, then it tends toward the reference value within the distance r. Accordingly, the diffusion current density contribution (not shown) approaches zero in the mixing points, then tends to the

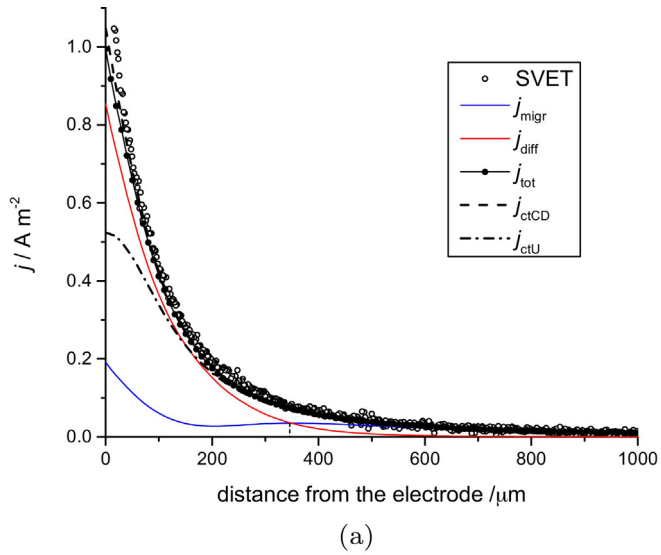

Fig. 8. Total, diffusion and migration components of current density in the solution simulated without accounting for the local mixing effect in comparison to the analytical distribution above the center of the electrode and SVET measurements under (a) anodic and (b) cathodic polarizations ($I = \pm 60$ nA).

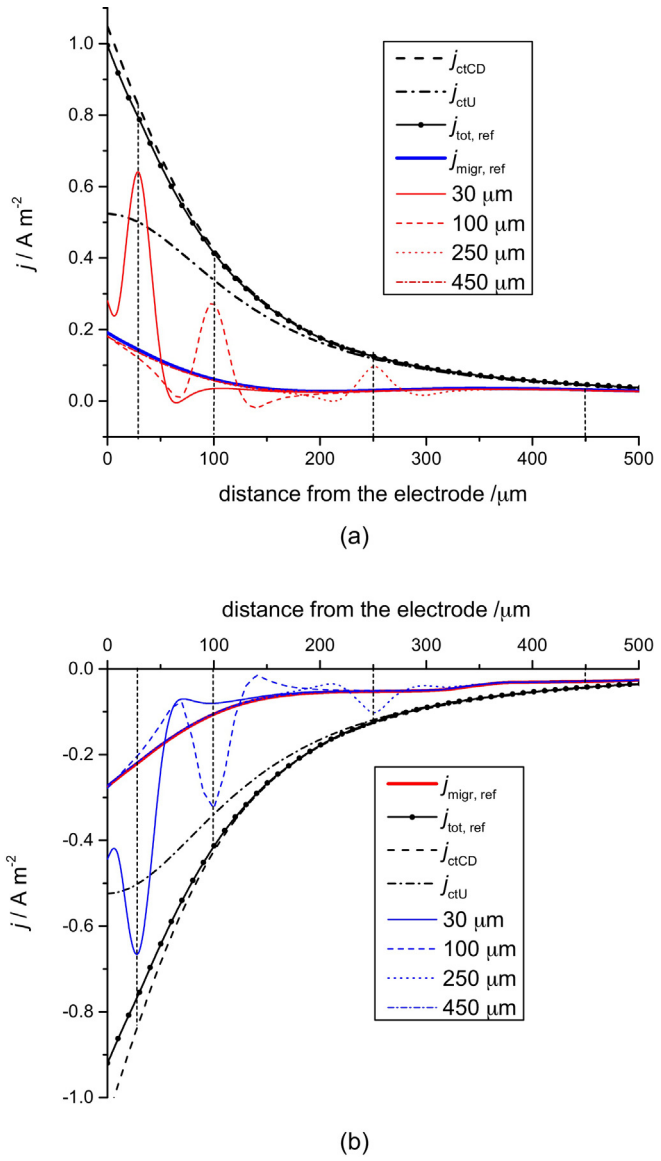

Fig. 9. The effect of the local mixing on the distribution of the ohmic current density for the mixing point at 30, 100, 250 and 450 μm above the center of the electrode under (a) anodic and (b) cathodic polarizations ($I = \pm 60$ nA). Vertical dashed lines indicate the position of mixing points.

reference value. Note, that the effect of the local mixing on the diffusion and migration contributions is the most pronounced close to the electrode surface, where the concentration gradients are the highest. Outside the diffusion layer, at 450 μm, the electrolyte is fully mixed, therefore no alteration of the contributions to current transport is predicted. Although the migration and diffusion contributions are altered locally, the total current density distribution is not altered, it stays the same as for the reference case.

Aside from the local reduction of the concentration gradients, the local mixing has no significant influence on the distribution of the species in the electrolyte solution. For illustration, the simulated distributions of pH and dissolved oxygen above the center of the electrode under both anodic and cathodic polarization are presented in Fig. 10, for the reference case and different points of local mixing. Corresponding measured values of pH and oxygen concentration are also shown there for comparison. One can observe that there is a good agreement between simulated and measured pH distributions obtained under anodic polarization for all distances from the electrode, as well as at distances larger than ±325 μm under cathodic polarization. At the same time, closer to the electrode the simulated pH values are overestimated (see Fig. 10(a)). A possible reason for such an overestimation can be the fact that the dissolved CO_2, which acts as a buffer due to formation of hydrocarbonate ions, is not taken into account in the present model. However, this does not influence the main conclusion. Note that in the mixing point there is no pH deviation from the reference value. A slight flattening of the pH profile is predicted around the mixing point, but is limited by the value of r. This finding is very important for the validation of the quasi-simultaneous SVET-pH measurements procedure developed by some of the authors [12].

The simulated and measured oxygen distributions obtained for anodic and cathodic polarizations are shown in Fig. 10(b). Note that in order to eliminate an effect of the difference between the oxygen bulk concentrations assumed in the model and measured experimentally, the O_2 concentrations values were corrected with respect to $[O_2]^{bulk}$. One can see that the model is able to reproduce the measured oxygen distributions with good precision. Furthermore, the model predicts a local increase of oxygen concentration on the

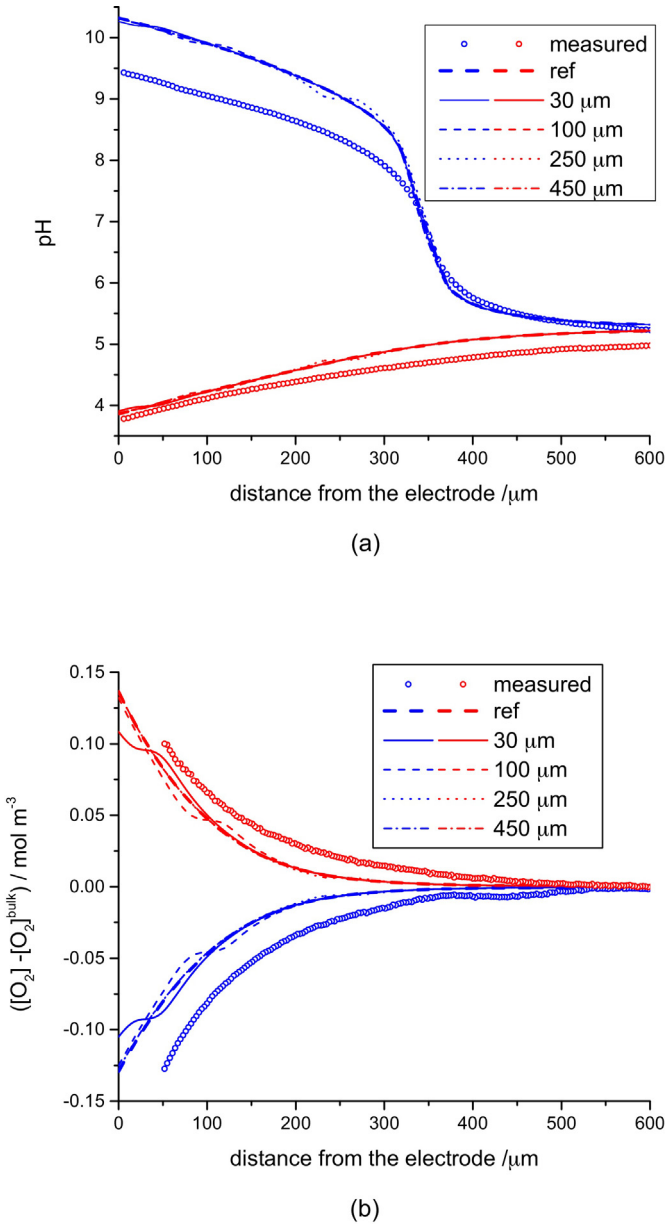

Fig. 10. Simulated (lines) pH and oxygen distributions above the center of the electrode for different positions of the mixing point, under anodic (red) and cathodic (blue) polarizations ($I = \pm 60$ nA). Corresponding measured values are shown as dots.

electrode surface when the SVET probe is close to the electrode (mixing point 30 μm). Remark that this increase is seen only at the centre of the disc where the SVET is placed and that this local effect will not much influence the total potential response [13]. Such an increase of concentration is expected and confirms experimental observations [10], although they were performed in totally different conditions.

6. Conclusions

We propose an elegant and accessible way to account in a multi-ion model for the local stirring created by the vibration of the SVET tip, without solving for the fluid flow. It is achieved by adding into the molar flux expression a new space dependent diffusion-like term $-D_{\mathrm{loc}}\bar{\nabla}c_i$ that accounts for the local mixing. This term is maximal in the point of vibration and rapidly decreases with the distance. The proposed model reflects much better the experimental data and might be an explanation why the analytical (ohmic) total current density is measured also in the regions where the diffusion contribution would be expected in the standard Multi-Ion model.

Performed simulations show that the local mixing caused by the vibrating SVET tip leads to a substantial increase of the migration current density in the vicinity of the probe with simultaneous decrease of the diffusion current density contribution, both for anodic and cathodic polarizations. At the same time this does not influence the total current density. Further, the simulations demonstrate that vibration only affects locally the pH distribution, regardless the applied polarization. One can say that the global diffusion behavior is not disarranged. Being close to the electrode surface, the vibration leads to a substantial but very local increase of the oxygen concentration under cathodic polarization. When the tip of the SVET probe is small compared to the size of the electrode, this effect will be negligible. These results show the validity of a quasi-simultaneous SVET and pH measurement procedure. SVET probes being large compared to the size of the electrode will influence the response of the system.

The proposed modeling approach is still rather qualitative as arbitrary parameters, without a direct physical meaning, are used for the description of the local mixing contribution. In order to make it quantitative, the local mixing parameters need to be linked to physical quantities based on flow calculations and/or measurements. Nevertheless, even in its present state this approach can be used for the description of the phenomena taking place in presence of the vibrating probe while avoiding the ambiguity between the Potential model and Multi-Ion model.

Acknowledgements

Present work was supported by FP7 Marie Curie IRSES project SISET, FP7-PEOPLE-IRSES-GA-2010-269282 and RFCS project AtCorAS, 2011-CT-2011-00015, and the cotutelle VUB-TUCN post-doc agreement. Sviatlana V. Lamaka thanks the Alexander von Humboldt foundation for its financial support of her Experienced Research Grant.

References

[1] H. Isaacs, The use of the scanning vibrating electrode technique for detecting defects in ion vapor-deposited aluminum on steel, Corrosion 43 (10) (1987) 594–596, http://dx.doi.org/10.5006/1.3583835.
[2] C. Crowe, R. Kasper, Ionic current densities in the nearfield of a corroding iron-copper galvanic couple, Journal of the Electrochemical Society 133 (1986) 879–887.
[3] D. Worsley, H. McMurray, A. Belghazi, Determination of localised corrosion mechanisms using a scanning vibrating reference electrode technique, Chemical Communications (1997) 2369–2370, http://dx.doi.org/10.1039/A704530A.
[4] A. Bastos, M. Ferreira, A. Simoes, Corrosion inhibition by chromate and phosphate extracts for iron substrates studied by EIS and SVET, Corrosion Science 48 (6) (2006) 1500–1512, http://dx.doi.org/10.1016/j.corsci.2005.05.021.
[5] R. Souto, J. Izquierdo, J. Santana, S. Gonzalez, Scanning microelectrochemical techniques. A highly sensitive route to evaluate degradation reactions and protectionmethodes with chemical selectivity, European Journal of Science and Theology 9 (2) (2013) 71–89.
[6] M. Mouanga, F. Andreatta, M.-E. Druart, E. Marin, L. Fedrizzi, M.-G. Olivier, A localized approach to study the effect of cerium salts as cathodic inhibitor on iron/aluminum galvanic coupling, Corrosion Science 90 (2015) 491–502, http://dx.doi.org/10.1016/j.corsci.2014.03.026.
[7] L. Jaffe, R. Nuccitelli, An ultrasensitive vibrating probe for measuring steady extracelular currents, The Journal of Cell Biology 63 (1974) 614–628.
[8] J. Ferrier, W. Lucas, Ion transport and the vibrating probe, Biophysical Journal 49 (1986) 803–806.
[9] J. Ferrier, W. Lucas, Theory of ion transport and the vibrating probe, Ionic Currents in Development (1986) 45–52.
[10] H. McMurray, D. Williams, D. Worsley, Artifacts induced by large-amplitude probe vibrations in localized corrosion measured by SVET, Journal of The Electrochemical Society 150 (2003) B567–B573, http://dx.doi.org/10.1149/1.1623494.

[11] A. Bastos, M. Zheludkevich, M. Ferreira, A SVET investigation on the modification of zinc dust reactivity, Progress in Organic Coatings 63 (2008) 282–290, http://dx.doi.org/10.1016/j.porgcoat.2008.01.013.
[12] S. Lamaka, M. Taryba, M. Montemor, H. Isaacs, M. Ferreira, Quasi-simultaneous measurements of ionic currents by vibrating probe and pH distribution by ion-selective microelectrode, Electrochemistry Communications 13 (1) (2011) 20–23, http://dx.doi.org/10.1016/j.elecom.2010.11.002.
[13] A. Bastos, M. Quevedo, M. Ferreira, The influence of vibration and probe movement on SVET measurements, Corrosion Science 92 (2015) 309–314, http://dx.doi.org/10.1016/j.corsci.2014.10.038.
[14] H. Isaacs, The measurement of the galvanic corrosion of soldered copper using the scanning vibrating electrode technique, Corrosion Science 28 (6) (1988) 547–558, http://dx.doi.org/10.1016/0010-938X(88)90023-6.
[15] E. Bayet, F. Huet, M. Keddam, K. Ogle, H. Takenouti, Local electrochemical impedance measurement: scanning vibrating electrode technique in ac mode, Electrochimica Acta 44 (1999) 4117–4127.
[16] F. Thebault, B. Vuillemin, R. Oltra, C. Allely, K. Ogle, Reliability of numerical models for simulating galvanic corrosion processes, Electrochimica Acta 82 (2012) 349–355, http://dx.doi.org/10.1016/j.electacta.2012.04.068.
[17] J. Newman, Current distribution on a rotating disk below the limiting current, Journal of the Electrochemical Society 113 (1966) 1235–1241.
[18] H. Isaacs, The effect of height on the current distribution measured with a vibrating electrode probe, Journal of the Electrochemical Society 138 (1991) 722–728.
[19] J. Newman, K.E. Thomas-Aleya, Electrochemical Systems, third edition, John Wiley & Sons, Inc, New Jersey, Hoboken, 2004.
[20] V. Topa, A. Demeter, L. Hotoiu, D. Deconinck, J. Deconinck, A transient multi-ion transport model for galvanized steel corrosion protection, Electrochimica Acta 77 (2012) 339–347, http://dx.doi.org/10.1016/j.electacta.2012.06.021.
[21] D. Deconinck, S. Van Damme, J. Deconinck, A temperature dependent multi-ion model for time accurate numerical simulation of the electrochemical machining process., Part II: Numerical simulation, Electrochimica Acta 69 (2012) 120–127, http://dx.doi.org/10.1016/j.electacta.2012.02.079.
[22] C. Amatore, S. Szunerits, L. Thouin, J.-S. Warkocz, The real meaning of Nernst's steady diffusion layer concept under non-forced hydrodynamic conditions. a simple model based on Levich's seminal view of convection, Journal of Electroanalytical Chemistry 50 (2001) 62–70.
[23] O. Dolgikh, A.S. Demeter, A.C. Bastos, V. Topa, J. Deconinck, A practical way to model convection in non-agitated electrolytes, Analytical Chemistry 37 (2013) 20–23, http://dx.doi.org/10.1016/j.elecom.2013.10.002.
[24] C. Scheffey, Two aproaches to construction of vibrating probes for electrical current measurement in solution, Review of Scientific Instruments 59 (1988) 787–792.
[25] G. Platt, I. Bastos, M. de Andrade, M. Taryba, S. Lamaka, A. Simoes, G. Soares, Thermodynamic simulation of phosphate precipitation based on ion-selective microelectrode measurements, Journal of the Brazilian Chemical Society 24 (2013) 1064–1071.
[26] M. Taryba, K. Van den Bergh, J. De Strycker, O. Dolgikh, J. Deconinck, S. Lamaka, Novel use of a micro-optode in overcoming the negative influence of the amperometric micro-probe on localized corrosion measurements, Corrosion Science 95 (2015) 1–5.
[27] M. Taryba, M. Montemor, S. Lamaka, Quasi-simultaneous mapping of local current density, pH and dissolved O_2 (2015), http://dx.doi.org/10.1002/elan.201500286.
[28] W. Stumm, J. Morgan, Aquatic Chemistry: Chemical Equilibria and Rates in Natural Waters, John Wiley & Sons Inc, 1996.